Subsurface Sensing Technologies and Applications Vol. 4, No. 1, January 2003 (©2003)

Improved Three-dimensional Image Reconstruction Technique for Multi-Component Ground Penetrating Radar Data

J. van der Kruk,*† C. P. A. Wapenaar, J. T. Fokkema, and P. M. van den Berg

Centre for Technical Geoscience, Delft University of Technology,
P.O. Box 5028, 2600 GA Delft, The Netherlands

Received April 2, 2002; revised August 23, 2002

For electromagnetic imaging the vectorial character of the emitted field and the radiation characteristics of both source and receiver play an important role. Recently, a new imaging algorithm was presented dedicated to the electromagnetic case. The radiation characteristics of GPR source and receiver antennas and the vectorial nature of the electromagnetic waves are taken into account for a monostatic fixed offset GPR survey. This resulted in a representative image of a point scatterer. Comparison with scalar imaging algorithms shows that for a homogeneous space the SAR image has an opposite sign compared to the multi-component image, whereas the Gazdag image has a phase shift of about 90° with respect to the multi-component image. In this paper, modified scalar imaging algorithms are introduced that minimize these differences. However, between the images obtained in a homogeneous half-space phase differences of 10–20° are still present. These differences indicate the possible error in nature of the physical property contrast when it is determined with the modified scalar imaging algorithms. The multi-component imaging algorithm returns a representative image because it uses the appropriate Greens functions to eliminate the propagation effects. For practical imaging strategies, only far-field radiation characteristics can be used to compensate for the propagation effects due to the large computing time needed to evaluate the total-field expressions. Synthetic analysis of the imaging of a point scatterer calculated using total-field expressions shows that using the far-field expressions in the multi-component imaging algorithm the images better approximate the actual contrast than using the modified scalar imaging algorithms. Experimental results are presented from imaging several buried objects with different medium properties and different orientations. The phase differences in the experimental data are similar to those obtained synthetically. This likeness indicates that using the multi-component imaging algorithm, a more reliable image is obtained than with the modified scalar imaging algorithms.

Key Words. GPR, 3D, imaging, multi-component, modified scalar imaging algorithms, total-field, far-field.

*To whom all correspondence should be addressed. Phone: +41 1 6332659; fax: +41 1 6331065; e-mail: jvdmk@aug.ig.erdw.ethz.ch

†Now at the Institute of Geophysics, ETH-Hoenggerberg, CH 8093, Zurich, Switzerland.

1566-0184/03/0100-0061/0 © 2003 Plenum Publishing Corporation

1. Introduction

Ground Penetrating Radar (GPR) is an electromagnetic high resolution tool, that has been employed successfully to perform numerous environmental, engineering and archaeological investigations [1]. Commonly used imaging strategies for GPR data used in the literature are similar to the (scalar) seismic processing algorithms. A tutorial paper [2] mentions that three methods of wavefield extrapolation, which describe the propagation effects of the wavefield, are commonly used in seismics, i.e., the Kirchhoff-summation approach [3], the plane-wave method (k–f method) [4], and the finite-difference technique. The forward and inverse wavefield extrapolation of single- and multi-component seismic data is described in [5].

Because of similarities between acoustic and electromagnetic prospecting methods, seismic imaging techniques were initially used for the imaging of GPR data [6,7,8,9,10,11]. However, there are also important differences between acoustic and electromagnetic prospecting methods. The most important difference is the vectorial character of electromagnetic waves compared to the scalar acoustic waves.

For a GPR measurement, the source and receiver are usually present on the interface between air and ground. This causes angle-dependent amplitude and polarization variations in the vectorial radiation characteristics of an elementary antenna [12,13]. Recently, these radiation characteristics of elementary GPR antennas for GPR data imaging have been taken into account. A modified Kirchhoff integral is used by inclusion of a half-space interfacial radiation pattern in [14]. Coincidental georadar data sets were combined with two pairs of parallel source-receiver antennas, one oriented perpendicular to the other to obtain a ''pseudo scalar'' wavefield [15]. Next, this pseudo scalar wavefield was imaged using a standard 3-D Kirchhoff time-migration scheme. A regular Kirchhoff migration was modified in [16] by limiting the migration to those paths that are within the predicted angle of orientation. However, all these algorithms were still adapted from scalar imaging algorithms and use the knowledge of the radiation characteristics of elementary GPR antennas heuristically to obtain a better image. A vectorial GPR imaging algorithm was derived using the generalized Radon transform [17]. However, the forward model that is used in the imaging operator does not fully account for variations of amplitude.

Recently, a multi-component imaging algorithm is presented [18], which is dedicated to the electromagnetic case. Improved images were obtained for a monostatic fixed offset GPR survey by properly taking into account the polarization of the emitted and measured wavefield and the radiation characteristics of the source and receiver. Comparison of the

results of this new imaging algorithm, the multi-component imaging algorithm, with two of the scalar imaging algorithms ; the SAR imaging algorithm and the Gazdag phase shift method showed that in a homogeneous space the SAR image has an opposite sign (phase shift of 180°), whereas the Gazdag has a phase shift of 90°.

In this paper, modified scalar imaging algorithms are introduced that minimize these phase shifts of 90° and 180°. Note that the SAR and Gazdag imaging algorithms are based on the scalar scattering representation. For practical imaging strategies, when the source and receiver are present on a dielectric medium, only far-field radiation characteristics can be used in the multi-component imaging algorithm to eliminate the propagation effects due to the large computing time needed to evaluate the total-field expressions. In this paper, the effect of using these far-field expressions is investigated by calculating the response for a point scatterer using total-field expressions and imaging with the far-field expressions.

First, the far-field and total-field expressions for a dipole in a homogeneous space and homogeneous half-space are compared. After calculating the scattered electric field for a point source using the far- and total-field expressions and discussing the analytical results for the imaging of a point scatterer, the modified scalar imaging algorithms are introduced. Next, the imaging is performed for a point scatterer by using the modified SAR, modified Gazdag and multi-component imaging algorithm. The scattered field of the point scatterer is calculated using the total-field expressions and the multi-component imaging is performed using both the far- and total-field expressions. Finally, we present scalar and multi-component images computed from experimental field data.

2. Forward Model

To specify position in the used configuration we employ the coordinates (x_1, x_2, x_3) with respect to a fixed, right-handed, orthogonal, Cartesian reference frame with origin $\mathcal{O}$ and with three orthogonal base vectors $(\boldsymbol{i}_1, \boldsymbol{i}_2, \boldsymbol{i}_3)$, where $\boldsymbol{i}_3$ is pointing downwards. The subscript notation is chosen to describe the relations between the wavefield vectors and medium properties. Any repeated subscript implies the application of the summation convention. In this way, the position in our configuration may be written as $\boldsymbol{x} = x_1\boldsymbol{i}_1 + x_2\boldsymbol{i}_2 + x_3\boldsymbol{i}_3$ or $\boldsymbol{x} = x_p\boldsymbol{i}_p$ with $p \in \{1, 2, 3\}$ and $x \in \mathbb{R}^3$.

The configuration for the forward source problem consists of an unbounded inhomogeneous medium $\mathbb{D}$ with known electromagnetic properties. In this medium, sources are present that occupy the bounded domain $\mathbb{D}^e$, being a subdomain of $\mathbb{D}$. The electric field (E_k^i) values in all space are

obtained as

$$\hat{E}_k^i(\boldsymbol{x}^R, \omega) = \int_{\boldsymbol{x} \in \mathbb{D}^e} \hat{G}_{kr}^{EJ}(\boldsymbol{x}^R | \boldsymbol{x}, \omega) \hat{J}_r^e(\boldsymbol{x}, \omega)\, dV, \tag{1}$$

where $\boldsymbol{x}^R \in \mathbb{D}$. Latin subscripts can take the values $\{1, 2, 3\}$. Equation (1) shows that the electromagnetic field from a known electric (J_r^e) source in a known medium can be calculated in all space once the fields radiated by an appropriate point source (the Green's tensor function, $\hat{G}_{kr}^{EJ}$) has been calculated.

Many environmental and engineering targets of interest are located within a few wavelengths of the antennas. It is important that the behavior of the propagation of the electromagnetic field is known in this region. The total-field expressions describe the propagation of the electromagnetic field very accurately. For a homogeneous half-space they have to be obtained by evaluation of integral expressions which is a time consuming task. For a fast and efficient imaging algorithm, it is indispensable to have closed-form expressions of the electromagnetic field and therefore the far-field expressions are commonly used. The total- and far-field expressions for the electromagnetic field are compared for a homogeneous space and a homogeneous half-space.

2.1. Electromagnetic Field in Homogeneous Space

The total-field expression for the Greens function $\hat{G}_{kr}^{EJ}(\boldsymbol{x}^R | \boldsymbol{x}, \omega)$ in a homogeneous space can be written as $\hat{G}_{kr}^{EJ}(\boldsymbol{x}^R - \boldsymbol{x}, \omega)$ and is given by

$$\hat{G}_{kr}^{EJ}(\boldsymbol{x}, \omega) = \hat{\eta}^{-1}[\partial_k \partial_r + k^2 \delta_{kr}] \hat{G}(R, \omega), \tag{2a}$$

$$\hat{G}(R, \omega) = \frac{\exp(-jkR)}{4\pi R}, \tag{2b}$$

$$R = |\boldsymbol{x}|, \tag{2c}$$

$$k = \frac{\omega}{c}, \tag{2d}$$

where c is the propagation velocity and $\omega = 2\pi f$ and $\exp(-jkR)$ is the propagation factor. Due to the spatial derivatives, particular direction patterns arise, which depend on the orientation of the source and the direction of observation. Another fact that arises due to the spatial derivatives is that the field can be divided in three different contributions ; the near field is proportional to $|\boldsymbol{x}|^{-3}$, the intermediate field proportional to $|\boldsymbol{x}|^{-2}$ and the far field proportional to $|\boldsymbol{x}|^{-1}$ [19]. These closed form representations facilitate

a thorough analysis of the radiation characteristics of each separate near, intermediate- and far-field term. For $|kR| \gg 1$, the near and intermediate field can be neglected compared to the far-field contributions.

We will concentrate on the amplitudes of the electric field in spherical coordinates (R, ϕ, θ). The analysis is carried out in two planes ; the E-plane ($\phi = 0$), and the H-plane ($\phi = \pi/2$). The E-plane is parallel to the direction of the current source dipole, while the H-plane is perpendicular to it. The configuration is given in Figure 1(a). The electric current source is positioned at the origin and is oriented in the $\boldsymbol{i}_1$-direction ($\phi = 0$). For different

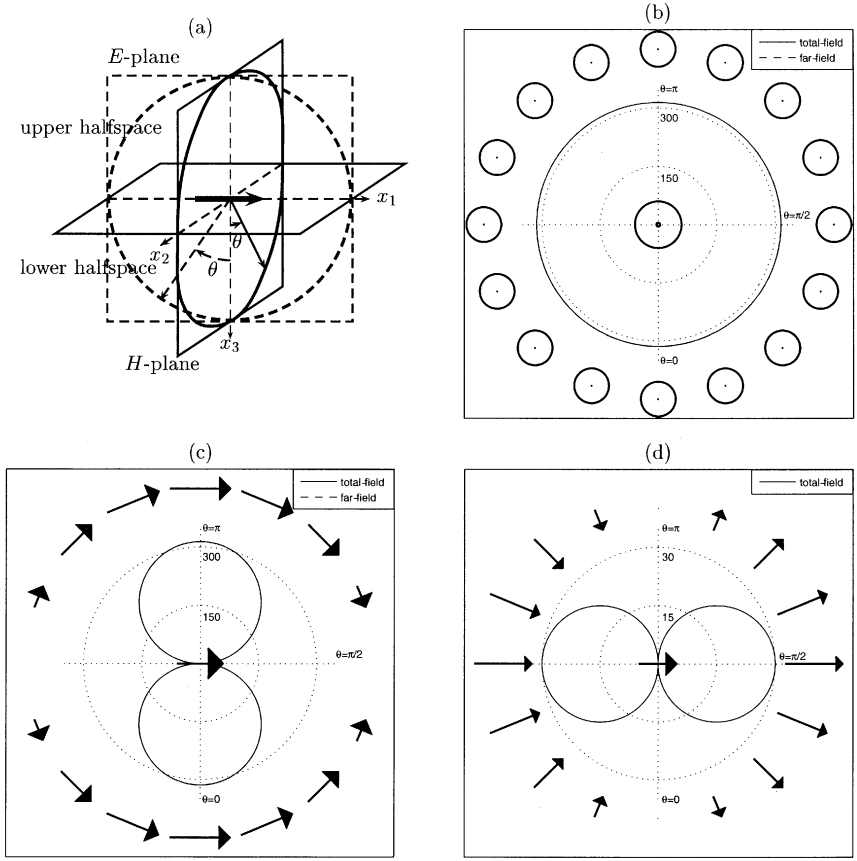

Figure 1. (a) Different planes of investigation ; the E-plane and the H-plane. The amplitude of the total- and far-field amplitudes for (b) $\hat{E}_\phi$ in the H-plane and (c) $\hat{E}_\theta$ and (d) $\hat{E}_R$ in the E-plane for $R = 1\,\text{m} \approx 3.3\lambda$, $f = 500\,\text{MHz}$, $\sigma = 0\,\text{S/m}$, and $\varepsilon_r = 4$. The orientation of the field is indicated by the symbol $\odot$ and an arrow.

angles θ the electric field is analyzed at a fixed radius of 1 m, which is $\approx 3.3\lambda$ for $f = 500$ MHz and a relative permittivity of $\varepsilon_r = 4$. This is a representative distance of a possible scatterer with respect to the position of the source and receiver antennas.

The amplitude and polarization of the electric total- and far-field are plotted in Figure 1(b,c) for the *H*- and the *E*-plane, respectively. In Figure 1(b) a circle is present in the origin, indicating the direction of the source, which is perpendicular to the *H*-plane and in Figure 1(c) an arrow is present in the origin of the *E*-plane, indicating the direction of the source, which is parallel to the *E*-plane. The solid and dashed lines indicate the amplitude of the electric total- and far-field, respectively. The dotted circles indicate equal amplitudes. The only component of the electric field in the *H*-plane is in the $\boldsymbol{i}_1$-direction and is omnidirectional. The electric field components in the *E*-plane are in the $\boldsymbol{i}_1$- and $\boldsymbol{i}_3$-direction. $\hat{E}_\theta$ has a zero for $x_3 = 0$ in the *E*-plane. Because $|kR| = 20\pi/3 \gg 1$, the near- and intermediate-field have a low amplitude compared to the far-field and the contribution of the near- and intermediate-field to $\hat{E}_\phi$ and $\hat{E}_\theta$ can be neglected. The difference between the total- and far-field was about 0.1% and not distinguishable in Figures 1(b,c). The electric field shown in Figures 1(b,c) contributes to the radiated power. However, it is still important to know also the electric field in the radial direction ($\hat{E}_R$), which is shown for the *E*-plane in Figure 1(d). $\hat{E}_R$ is zero in the *H*-plane ($x_1 = 0$). In the *E*-plane, $\hat{E}_R$ has no far-field contribution and is mainly proportional to $|\boldsymbol{x}|^{-2}$ and thus mainly due to the intermediate field. The maximum amplitude for $\hat{E}_R$ is a factor 10 less compared to the amplitude for $\hat{E}_\phi$ and $\hat{E}_\theta$ for the parameters used in this analysis ($|kR| = 20\pi/3$) and may have to be taken into account for a scatterer that is relatively close to the source and receiver antennas.

2.2. Electromagnetic Field in Homogeneous Half-Space

Far-field asymptotic solutions for a lossless half-space are given in [13]. Total-field solutions are obtained by numerically evaluating the integral equations using standard integration routines [20]. The same configuration is used as is given in Figure 1(a). However, now a dielectric medium ($\varepsilon_r = 4$) is present for $0 < \theta < \pi/2$, while for $\pi/2 < \theta < \pi$ air is present. The different contributions to the total-field are shown in Figure 2(a). The far-field expressions only describe the body wave in air and ground and have a zero at the interface, whereas the total-field expressions also describe the head wave in the ground and the inhomogeneous wave in air. The critical angle θ_c is given by $\theta_c = \sin^{-1}(1/\sqrt{\varepsilon_r})$ for a lossless medium. For different angles θ the two expressions for the electric field are compared.

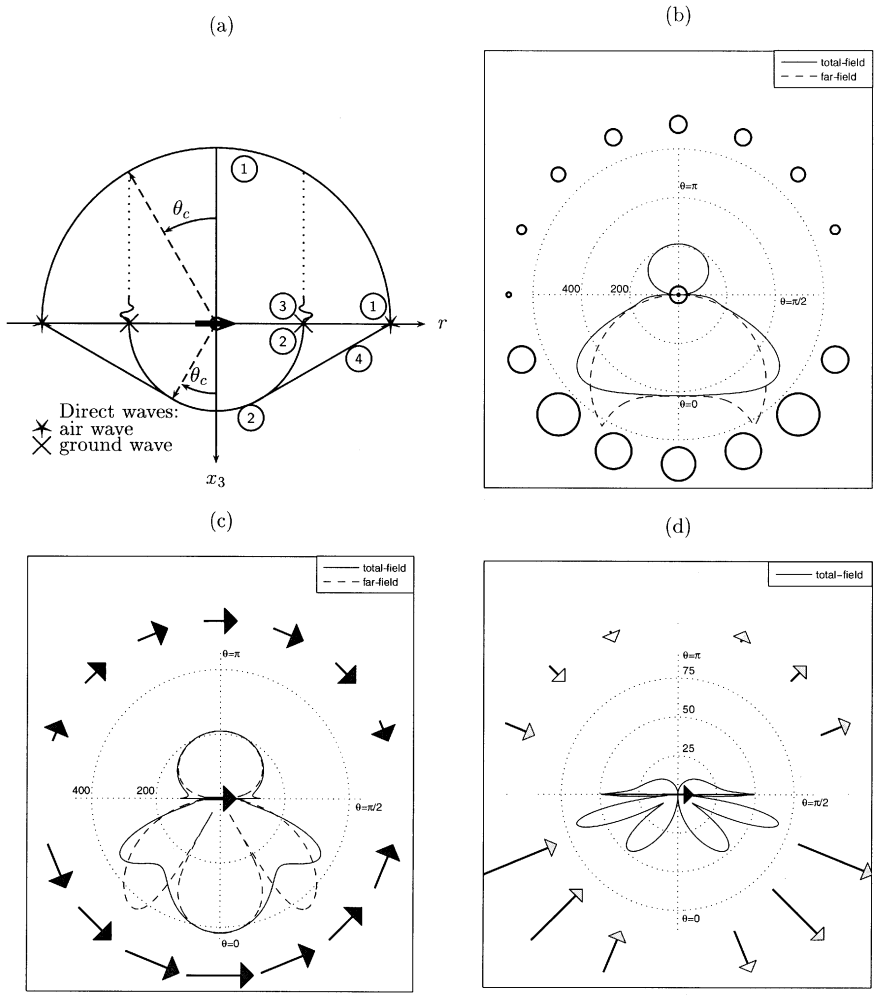

Figure 2. (a) Wavefronts generated by a dipole source on the surface of a half-space earth with 1: Body wave in air, 2: Body wave in ground, 3: Inhomogeneous wave in air, and 4: Head wave in ground. Comparison between the total-field and far-field amplitudes of the spherical electric field component, (b) $\hat{E}_\phi$ in the H-plane, and (c) $\hat{E}_\theta$, and (d) $\hat{E}_R$ in the E-plane for $R = 1\,\text{m} \approx 3.3\lambda$, $f = 500\,\text{MHz}$, $\sigma = 0\,\text{S/m}$, and $\varepsilon_r = 4$.

In Figure 2(b–d) the far-field and the total-field spherical electric components are depicted at a radius of $1\,\text{m} \approx 3.3\lambda$ for $f = 500\,\text{MHz}$. $\hat{E}_\phi$ in the H-plane is depicted in Figure 2(b) and $\hat{E}_\theta$ and $\hat{E}_R$ in the E-plane are depicted in Figures 2(c,d), respectively. It is observed that the far-field

expressions do not resemble the total-field in the lower half-space at the critical angle (θ_c), where the far-field result has a maximum amplitude in the H-plane and a minimum amplitude in the E-plane. $\hat{E}_R$ has no far-field contribution. The maximum amplitude for $\hat{E}_R$ is a factor 7 less compared to the amplitude for $\hat{E}_\phi$ and $\hat{E}_\theta$. This indicates that for a homogeneous half-space the intermediate field has a larger amplitude than in a homogeneous space.

The large contribution of the intermediate field near the critical angle (θ_c), which also contains the head wave that is not incorporated in the far-field, causes the maximum of the radiation pattern for the total-field not to be present at the critical angle, but at an angle larger than the critical angle. Far-field expressions are compared to FDTD modeling in [21] and [22] and similar phenomenon are observed. Further research is needed to obtain closed-form expressions for the intermediate field, which eventually can be used for imaging purposes.

3. Scattering Formalism

We investigate the scattering of electromagnetic fields by a contrasting domain of bounded extent present in an unbounded homogeneous medium $\mathbb{D}$ that has a conductivity σ, permittivity ε, and permeability μ. $\mathbb{D}^s$ is the bounded domain occupied by the scatterer with conductivity $\sigma^s(\boldsymbol{x})$, permittivity $\varepsilon^s(\boldsymbol{x})$ and permeability $\mu^s(\boldsymbol{x}) = \mu$. The contrast source volume density $\hat{J}_k^s$ of electric current, also denoted as scatter source, is given by

$$\hat{J}_k^s = \chi^{\hat{\eta}} \hat{E}_k. \tag{3}$$

in which the medium contrast function is found as

$$\chi^{\hat{\eta}} = \hat{\eta}^s - \hat{\eta} = (\sigma^s - \sigma) + j\omega(\varepsilon^s - \varepsilon). \tag{4}$$

Once the total-field strengths ($\hat{E}_k$ in Eq. (3)) inside the scatterer are known, the scattered field values in all space can then be obtained upon substituting the relevant values for the scatter source into the following equation

$$\hat{E}_k^s(\boldsymbol{x}^R, \omega) = \int_{\boldsymbol{x} \in \mathbb{D}^s} \hat{G}_{kr}^{EJ}(\boldsymbol{x}^R - \boldsymbol{x}, \omega) \hat{J}_r^s(\boldsymbol{x}, \omega)\, dV, \tag{5}$$

which is similar to Eq. (1). Using the so-called first-Born approximation [23], we assume that

$$\hat{J}_k^s(\boldsymbol{x}, \omega) \approx \chi^{\hat{\eta}} \hat{E}_k^i(\boldsymbol{x}, \omega). \tag{6}$$

Substitution Eq. (6) into Eq. (5) yields

$$\hat{E}_k^s(\boldsymbol{x}^R, \omega) = \int_{\boldsymbol{x} \in \mathbb{D}^s} \hat{G}_{kr}^{EJ}(\boldsymbol{x}^R - \boldsymbol{x}, \omega) \hat{\chi}^{\eta}(\boldsymbol{x}) \hat{E}_r^i(\boldsymbol{x}, \omega)\, dV. \tag{7}$$

We assume that the incident electromagnetic field is generated by external point sources $\hat{J}_t^e = \hat{S}(\omega)\delta(\boldsymbol{x} - \boldsymbol{x}^S)b_t$, where $\hat{S}(\omega)$ represents the source wavelet for the electric current sources and b_t represents the orientation of the electric current source. Substitution in Eq. (1) enables that the incident electric field generated by these point sources can be written as

$$\hat{E}_r^i(\boldsymbol{x}^c, \omega) = \hat{G}_{rt}^{EJ}(\boldsymbol{x}^c - \boldsymbol{x}^S, \omega)\hat{S}(\omega)b_t. \tag{8}$$

Substitution of Eq. (8) and the expression for the scatter source, Eq. (6), into Eq. (5) yields the expressions for the scattered field due to a small contrast

$$\hat{E}_k^s(\boldsymbol{x}^R, \boldsymbol{x}^S, \omega) = \hat{S}(\omega) \int_{\boldsymbol{x}^c \in \mathbb{D}^s} \hat{G}_{kr}^{EJ}(\boldsymbol{x}^R - \boldsymbol{x}^c, \omega) \hat{\chi}^{\eta}(\boldsymbol{x}^c) \hat{G}_{tr}^{EJ}(\boldsymbol{x}^S - \boldsymbol{x}^c, \omega) b_t\, dV, \tag{9}$$

where we have used

$$\hat{G}_{rt}^{EJ}(\boldsymbol{x}^c - \boldsymbol{x}^S, \omega) = \hat{G}_{tr}^{EJ}(\boldsymbol{x}^S - \boldsymbol{x}^c, \omega). \tag{10}$$

The Green's tensor function $\hat{G}_{tr}^{EJ}(\boldsymbol{x}^S - \boldsymbol{x}^c)$ describes the propagation of the electric field from the primary electric-current source at $\boldsymbol{x}^S$ towards the scatterer at $\boldsymbol{x}^c$. Similarly, the Green's tensor function $\hat{G}_{kr}^{EJ}(\boldsymbol{x}^R - \boldsymbol{x}^c)$ describes the propagation of the electric field from the secondary electric-current source present at $\boldsymbol{x}^c$ towards the receiver located at $\boldsymbol{x}^R$.

Taking into account that the orientation of the source and receiver is parallel to the interface to obtain a better coupling, four different source-receiver combinations are possible. Eq. (9) reduces to

$$\hat{E}_\alpha^s(\boldsymbol{x}^R, \boldsymbol{x}^S, \omega) = \hat{S}(\omega) \int_{\boldsymbol{x}^c \in \mathbb{D}^s} \hat{\chi}^{\eta}(\boldsymbol{x}^c) \hat{G}_{\alpha r}^{EJ}(\boldsymbol{x}^R - \boldsymbol{x}^c, \omega) \hat{G}_{\beta r}^{EJ}(\boldsymbol{x}^S - \boldsymbol{x}^c, \omega) b_\beta\, dV, \tag{11}$$

where $\{\alpha, \beta\} = \{1, 2\}$. We assume that the source and receiver are present on the same horizontal plane, $\{\boldsymbol{x}^S, \boldsymbol{x}^R\} \in \mathbb{D}^{SR}$, where $x_3^S = x_3^R = 0$. The configuration is depicted in Figure 3.

The source and receiver coordinates are now written as $\boldsymbol{x}^S = \boldsymbol{x}^M - \boldsymbol{x}^H$ and $\boldsymbol{x}^R = \boldsymbol{x}^M + \boldsymbol{x}^H$, where $\boldsymbol{x}^M$ is the midpoint between the two antennas and $\boldsymbol{x}^H$ is half of the offset. Because four different source-receiver combinations are possible, we introduce $\hat{E}_{\alpha\beta}(\boldsymbol{x}^M, \boldsymbol{x}^H, \omega)$, where

$$\hat{E}_\alpha^s(\boldsymbol{x}^M + \boldsymbol{x}^H, \boldsymbol{x}^H - \boldsymbol{x}^H, \omega) = \hat{E}_{\alpha\beta}(\boldsymbol{x}^M, \boldsymbol{x}^H, \omega) b_\beta, \tag{12}$$

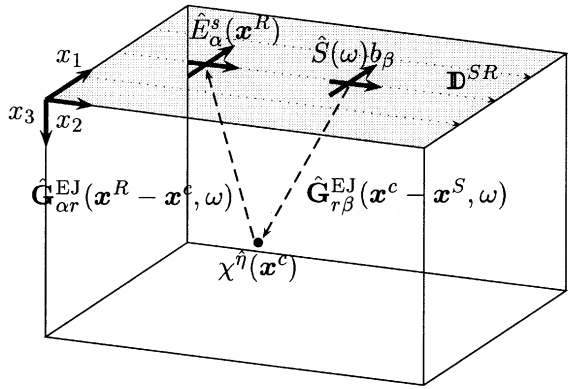

Figure 3. The configuration of the four possible source-receiver setups.

and $\hat{E}_{\alpha\beta}$ is given by

$$\hat{E}_{\alpha\beta}(\boldsymbol{x}^M, \boldsymbol{x}^H, \omega)$$

$$= \hat{S}(\omega) \int_{\boldsymbol{x}^c \in \mathbb{D}^s} \chi^{\hat{\eta}}(\boldsymbol{x}^c) \hat{G}^{EJ}_{\alpha r}(\boldsymbol{x}^M + \boldsymbol{x}^H - \boldsymbol{x}^c, \omega) \hat{G}^{EJ}_{\beta r}(\boldsymbol{x}^M - \boldsymbol{x}^H - \boldsymbol{x}^c, \omega)\, dV, \tag{13}$$

where α and β indicate the orientation of the receiver and the source, respectively. This notation is convenient when discussing the four different measurements separately.

Note that in this representation we have taken into account the polarization of the electromagnetic field that propagates through a homogeneous medium or homogeneous half-space. We have assumed that each point in the subsurface acts as an independent point diffractor and no multiples are present in the data. Using the Born approximation (valid for small contrast scatterers), linearized expressions of the scattered field are obtained which will be amenable to use as a starting point of the imaging procedure.

4. Modeling Results

To show the vectorial character and the influence of the radiation characteristics on the scattered field, synthetic results are calculated for a buried scatterer with a conductivity contrast using the scattering formalism as given in Eq. (13). The two Green's functions can be calculated using far-field and total-field expressions (as shown in Figures 1 and 2).

4.1. Measurements on an Acquisition Surface

For a buried point diffractor at $\boldsymbol{x} = (0, 0, 0.5)$, the scattered field is calculated at intervals of $\Delta x_1^M = \Delta x_2^M = 0.05$ m in both horizontal directions using the far-field expressions for an acquisition surface $-1.6 < x_1^M < 1.6$, $-1.6 < x_2^M < 1.6$ m, and $x_3^M = 0$ m for a frequency of 500 MHz in a homogeneous space and a homogeneous half-space ($\varepsilon_r = 4$) for a zero-offset ($\boldsymbol{x}^{\mathbf{H}} = \mathbf{0}$) source-receiver configuration.

In Figure 4(a,b) the calculated results are given for a homogeneous space for $\hat{E}_{11}$ and $\hat{E}_{21}$, respectively. Due to the radiation patterns of the source and receiver, more information is obtained for larger $|x_2|$ compared to $|x_1|$ for the perpendicular-broadside (co-pole) configuration ($\hat{E}_{11}$). The parallel–perpendicular (cross-pole) configuration ($\hat{E}_{21}$) shows a zero for $\{x_1, x_2\} = 0$.

In Figure 5(a,b) the calculated results are given for a homogeneous half-space for $\hat{E}_{11}$ and $\hat{E}_{21}$. Due to the radiation pattern of the source and receiver a maximum occurs for ($\hat{E}_{11}$) at the critical angle for $x_1 = 0$ and $x_2 = \{-0.6, 0.6\}$, while a minimum occurs at the critical angle for $x_2 = 0$ and $x_1 = \{-0.6, 0.6\}$. The parallel–perpendicular configuration ($\hat{E}_{21}$) shows again a zero for $\{x_1, x_2\} = 0$.

4.2. Measurements along an Acquisition Line in a Homogeneous Half-Space

Along the survey line, which is indicated in Figure 5(a,b), the scattered electric field in time domain was calculated for 21 positions with a stepsize $\Delta \boldsymbol{x}^M = (0, 0.05, 0)$ m, zero-offset configuration ($\boldsymbol{x}^H = (0, 0, 0)$) and starting at position $(0.25, -0.5, 0)$. A Gaussian wavelet was used as a source wavelet. The total-field and far-field results are presented for the perpendicular–broadside (E_{11}) and the parallel perpendicular (E_{21}) configuration in Figure 6(a,b), respectively. A significant difference between the total-field and the far-field is observed. This is due to the fact that the scatterer is located close to the source and receiver and as a consequence the far-field does not resemble the total-field. It is stressed that the measured reflections for positive and negative positions differ in sign for the cross-pole measurements shown in Figure 6(b).

5. Imaging

An imaging algorithm basically consists of two steps ; the first step corrects for propagation effects for each separate frequency component

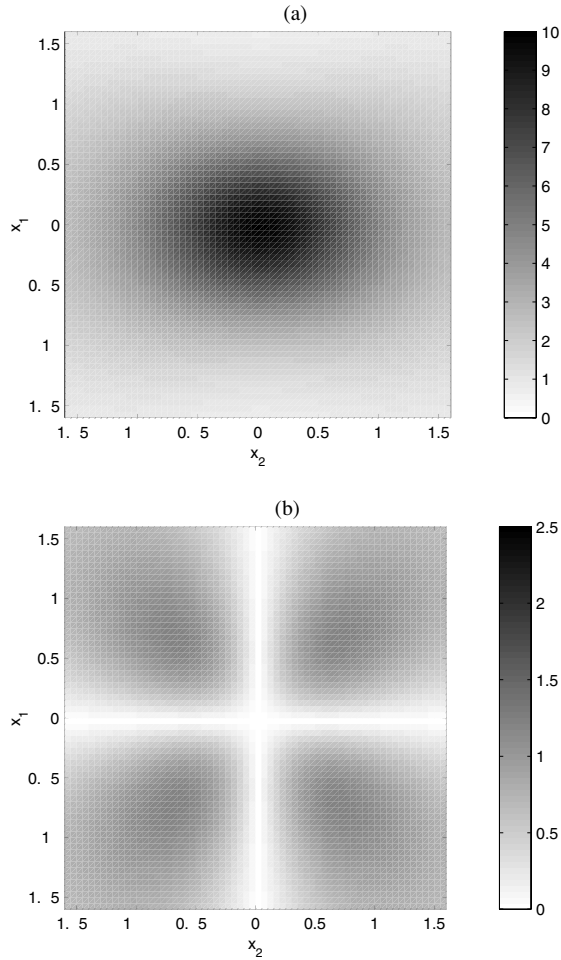

Figure 4. Far-field response for $f = 500$ MHz obtained from a buried point scatterer in a homogeneous space for (a) perpendicular–broadside $\hat{E}_{11}$ (co-pole) and (b) parallel–perpendicular $\hat{E}_{21}$ (cross-pole) configuration.

(inverse wavefield extrapolation). The second step involves a time zero selection for each position, which is carried out by adding all (positive and negative) frequencies. This operation is known as the imaging principle [24]. For all discussed imaging algorithms, the imaging principle is equivalent. The discussion of the inverse wavefield extrapolators is thus our main concern. To investigate the performance of scalar inverse extrapolators and to derive

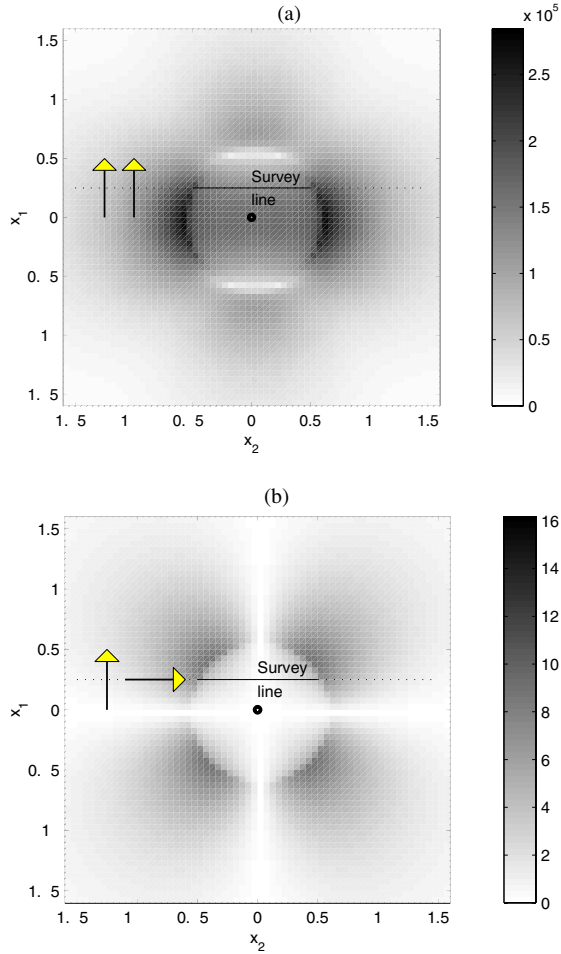

Figure 5. Far-field response for $f = 500$ MHz obtained from a buried point scatterer in a homogeneous half-space on a limited acquisition surface for (a) perpendicular–broadside configuration, $\hat{E}_{11}$ and (b) parallel–perpendicular configuration, $\hat{E}_{21}$.

systematically a bounded inverse extrapolator dedicated to the electromagnetic case, we first discuss the scattering formalism.

We rewrite the linearized expression for the scattering formalism $\hat{E}_{\alpha\beta}$, which is given by Eq. (13) as

$$\hat{E}_{\alpha\beta}(\boldsymbol{x}^M, \boldsymbol{x}^H, \omega) = \hat{S}(\omega) \int_{\boldsymbol{x}^c \in \mathbb{D}^s} \hat{D}_{\alpha\beta}(\boldsymbol{x}^M, \boldsymbol{x}^H, \boldsymbol{x}^c, \omega) \chi^{\hat{\eta}}(\boldsymbol{x}^c)\, dV, \qquad (14)$$

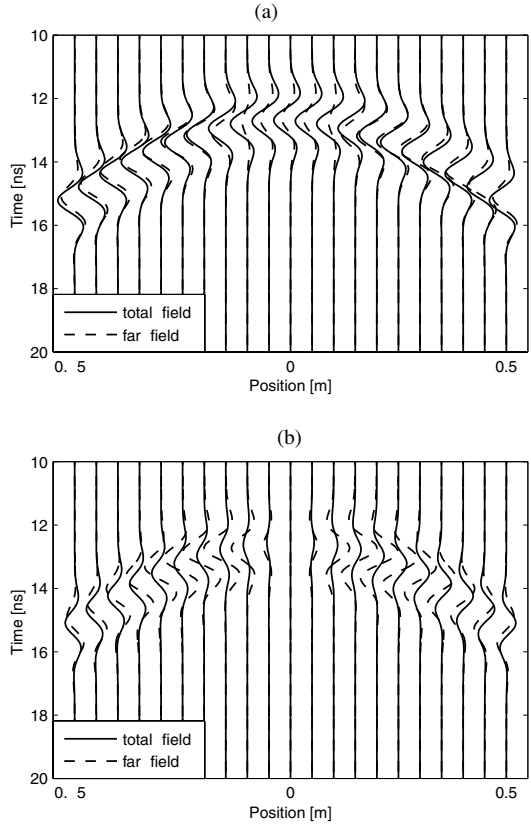

Figure 6. Comparison between total-field and far-field on survey line 1 for a σ-contrast using (a) perpendicular–broadside (co-pole) configuration and (b) parallel–perpendicular (cross-pole) configuration.

where the forward wavefield extrapolator $\hat{D}_{\alpha\beta}$ describes the inner product between the two Green's functions and is given by

$$\hat{D}_{\alpha\beta}(\boldsymbol{x}^M, \boldsymbol{x}^H, \boldsymbol{x}^c, \omega) = \hat{G}^{EJ}_{\alpha r}(\boldsymbol{x}^M + \boldsymbol{x}^H - \boldsymbol{x}^c, \omega)\hat{G}^{EJ}_{\beta r}(\boldsymbol{x}^M - \boldsymbol{x}^H - \boldsymbol{x}^c, \omega). \quad (15)$$

The forward wavefield extrapolator $\hat{D}_{\alpha\beta}$ describes the inner product of the Green's function describing the downward propagation from source towards scatterer and the Green's function describing the upward propagation from scatterer towards receiver in a homogeneous space or a homogeneous half-space.

To enable a thorough analytical discussion of the performance of the different inverse wavefield operators, we will first determine the forward

wavefield extrapolators in a lossless homogeneous space for a zero-offset configuration, with $\boldsymbol{x}^S = \boldsymbol{x}^R = \boldsymbol{x}^M = (x_1^M, x_2^M, 0)$, and $\boldsymbol{x}^H = 0$. Equation (14) can now be written as

$$\hat{E}_{\alpha\beta}(\boldsymbol{x}^M, \omega) = \hat{S}(\omega) \int_{\boldsymbol{x}^c \in \mathbb{D}^s} \hat{D}_{\alpha\beta}(\boldsymbol{x}^M - \boldsymbol{x}^c, \omega) \chi^{\eta}(\boldsymbol{x}^c)\, dV. \tag{16}$$

The expression for the Greens function in a homogeneous space, $\hat{G}_{kr}^{EJ}(\boldsymbol{x}, \omega)$, is given by Eq. (2a). The forward wavefield extrapolator can be rewritten by separating the phase delay and the corresponding amplitude factor as

$$\begin{aligned} \hat{D}_{\alpha\beta}(\boldsymbol{x}, \omega) &= \hat{G}_{\alpha r}^{EJ}(\boldsymbol{x}, \omega) \hat{G}_{\beta r}^{EJ}(\boldsymbol{x}, \omega), \\ &= \hat{A}_{\alpha\beta}(\boldsymbol{x}, \omega) \exp(-2jkR). \end{aligned} \tag{17}$$

Because the wavefield extrapolator in Eq. (17) is derived for a zero-offset measurement a factor 2 occurs in the two-way phase delay $\exp(-2jkR)$, which indicates that the wavefield has traveled twice along the same path. The separate elements of $\hat{A}_{\alpha\beta}$ in Eq. (17) are evaluated for the far-field contributions using Eqs. (2a)–(2d) and can be written as

$$\tilde{A}_{11}(\boldsymbol{x}, \omega) = \frac{R^2 - x_1^2}{R^4} C(\omega), \tag{18a}$$

$$\hat{A}_{12}(\boldsymbol{x}, \omega) = -\frac{x_1 x_2}{R^4} C(\omega), \tag{18b}$$

$$\hat{A}_{21}(\boldsymbol{x}, \omega) = -\frac{x_1 x_2}{R^4} C(\omega), \tag{18c}$$

$$\hat{A}_{22}(\boldsymbol{x}, \omega) = \frac{R^2 - x_2^2}{R^4} C(\omega), \tag{18d}$$

where

$$C(\omega) = \frac{k^4}{\hat{\eta}^2 (4\pi)^2}. \tag{19}$$

The zero-offset assumption in a homogeneous space enables a thorough analytical discussion of the performance of the different inverse wavefield extrapolators. In the following sections, the zero-offset assumption will hold.

5.1. Wavefield Extrapolator in Wavenumber-Frequency Domain

A horizontal spatial Fourier transformation is carried out using the stationary phase approximation to obtain the expression for $\hat{D}_{\alpha\beta}(x_1, x_2, x_3, \omega)$ in the wavenumber-frequency domain,* $\tilde{D}_{\alpha\beta}(k_1, k_2, x_3, \omega)$, yielding [18]

$$\tilde{D}_{\alpha\beta}(k_1, k_2, x_3, \omega) = \tilde{d}_{\alpha\beta} \exp(-jk_3|x_3|), \tag{20}$$

where k_3 is given by

$$k_3 = \begin{cases} \sqrt{4k^2 - k_1^2 - k_2^2}, & \text{for } k_1^2 + k_2^2 \leq 4k^2, \\ -j\sqrt{k_1^2 + k_2^2 - 4k^2}, & \text{for } k_1^2 + k_2^2 > 4k^2, \end{cases} \tag{21}$$

and

$$\tilde{d}_{11}(k_1, k_2, x_3, \omega) = -\frac{2\pi j C(\omega)}{(2k)^3|x_3|}[(2k)^2 - k_1^2], \tag{22a}$$

$$\tilde{d}_{12}(k_1, k_2, x_3, \omega) = \frac{2\pi j C(\omega)}{(2k)^3|x_3|} k_1 k_2, \tag{22b}$$

$$\tilde{d}_{21}(k_1, k_2, x_3, \omega) = \frac{2\pi j C(\omega)}{(2k)^3|x_3|} k_1 k_2, \tag{22c}$$

$$\tilde{d}_{22}(k_1, k_2, x_3, \omega) = -\frac{2\pi j C(\omega)}{(2k)^3|x_3|}[(2k)^2 - k_2^2]. \tag{22d}$$

Note that the method of stationary phase can also be applied to evaluate the inverse spatial Fourier transformation.

5.2. Scalar Inverse Wavefield Extrapolators

In this section, the relation between conventional scalar inverse wavefield extrapolators and the scattering formalism is shown. The symbol $\hat{H}$ is used to describe the different inverse wavefield extrapolators. We limit the number of extrapolators by only discussing imaging algorithms defined in the space-frequency or the wavenumber-frequency domain.

The phase shift of the forward wavefield extrapolator in the space-frequency domain as given in Eq. (17) yields

$$\exp(-2jkR) \tag{23}$$

*Also known as k–f domain, in this case we should actually speak of k_1, k_2, ω domain.

and the phase shift of the forward wavefield extrapolator in the wavenumber-frequency domain as given in Eq. (20) yields

$$\exp(-jk_3|x_3|), \tag{24}$$

where Eq. (21) indicates the region of the propagating waves and evanescent waves. It will be shown that the basis of conventional inverse wavefield extrapolators is to correct for the phase shift in either the space-frequency or horizontal Fourier domain.

5.2.1. Synthetic Aperture Radar Imaging

Synthetic Aperture Radar (SAR) imaging was originally developed for remote sensing [25]. This process is in many ways similar to the problem of seismic imaging of the earth's interior and is essentially a ray-tracing algorithm. In seismics, this imaging algorithm is known as diffraction summation migration. The inverse wavefield extrapolator for the SAR imaging algorithm is defined in the space-frequency domain and is the inverse of the phase shift given in Eq. (23)

$$\hat{H}^{\text{sar}}(\boldsymbol{x}, \omega) = \exp(2jkR). \tag{25}$$

The equivalent of Eq. (25) in the wavenumber-frequency domain is obtained by using the stationary phase approximation and is given by

$$\tilde{H}^{\text{sar}}(k_1, k_2, x_3, \omega) = \frac{4\pi jk|x_3|}{(k_3^*)^2} \exp(jk_3^*|x_3|). \tag{26}$$

Note that the inverse wavefield extrapolator in the wavenumber-frequency domain (Eq. (26)) has an increasing amplitude for increasing horizontal wavenumbers in the propagating wave region. Moreover, for wide angle measurements containing horizontal wavenumbers near the propagating and evanescent wave boundary, the amplitude of the inverse wavefield extrapolator is not bounded, because the denominator approaches zero, whereas the inverse wavefield extrapolator in the space-frequency domain (25) is bounded.

So a bounded expression in the space-frequency domain can be unbounded in the horizontal Fourier domain when it is determined using the stationairy phase approximation. Note that Eqs. (25) and (26) are related by the stationary phase approximation, which is based on the assumption of an infinite acquisition plane. The implementation in the space-frequency domain, which inherently is carried out for a bounded acquisition plane, results in a band limitation, which prevents amplitudes of the SAR inverse wavefield extrapolator becoming unbounded.

5.2.2. Gazdag Phase Shift Extrapolator

The Fourier transform method in seismic migration was introduced in [26]. A simple mapping from temporal frequency ω to vertical wavenumber k_3 involves interpolation for the required data samples. The phase-shift method was published in [4], which led to a further understanding of wavefield extrapolation in the transform domain. Since then, several names were introduced for the Gazdag phase shift method. Some of them are: backpropagation imaging, plane wave method or wavenumber-frequency migration. It was shown in [3] that the Kirchhoff integral extrapolator, which is defined in the space-time domain, is similar to the Gazdag phase shift extrapolator, which is defined in the horizontal Fourier domain for a specific combination of source and receiver types in the acoustic case. The Gazdag phase-shift is commonly used in combination with the exploding reflector assumption, which does not account correctly for geometrical spreading. The inverse wavefield extrapolator, which forms the basis of Gazdag phase-shift imaging [4], is defined in the horizontal Fourier domain and is an approximate inverse of the phase shift given in Eq. (24). To obtain a bounded inverse wavefield extrapolator, the complex conjugate of the vertical wavenumber is taken. In reality, this means that only the propagating wave region is used. The Gazdag inverse wavefield extrapolator is given by

$$\tilde{H}^{\mathrm{gd}}(k_1, k_2, x_3, \omega) = \exp(jk_3^*|x_3|). \tag{27}$$

Note, that within the propagating wave region the amplitude of the inverse wavefield extrapolator given in Eq. (27) is unity. Using the stationary phase approximation, the expression for this operator in the space-frequency domain is obtained as

$$\hat{H}^{\mathrm{gd}}(\boldsymbol{x}, \omega) = -\frac{jk|x_3|}{\pi R^2}\exp(2jkR). \tag{28}$$

5.3. Comparison of Scalar Inverse Wavefield Extrapolators

The SAR and Gazdag inverse wavefield extrapolators both consist of a phase shift of the original measured signal weighted with some frequency- and angle-dependent factors (Table 1). In the space-frequency domain, the phase shift is given by $\exp(2jkR)$ and in the wavenumber-frequency domain, it is given by $\exp(jk_3^*|x_3|)$.

The Gazdag and SAR operators are basically phase shifts in the space-frequency domain and in the wavenumber-frequency domain, respectively. Neither operator takes into account the vectorial character and the radiation characteristics of the source and receiver antennas.

Table 1. Overview of the Scalar Inverse Wavefield Extrapolators in the Space-Frequency ($x-\omega$) Domain and in the Wavenumber-Frequency Domain ($k-\omega$)

Inverse extrapolator	$x-\omega$ domain $\hat{H}$	$k-\omega$ domain $\tilde{H}$
SAR	$\exp(j2kR)$	$\frac{4\pi jk\lvert x_3\rvert}{(k_3^*)^2}\exp(jk_3^*\lvert x_3\rvert)$
Gazdag	$\frac{-jk\lvert x_3\rvert}{\pi R^2}\exp(2jkR)$	$\exp(jk_3^*\lvert x_3\rvert)$

Note that when these inverse wavefield extrapolators are known in both the space-frequency domain and the wavenumber-frequency domain, the wavefield extrapolation can be carried out in either the space-time domain, the space-frequency domain or the wavenumber-frequency domain. Each domain has its own limitations and advantages. When some topographic adjustments are needed, implementation in the wavenumber-frequency domain is not an option. Frequency-dependent medium parameters can be taken into account in the space-frequency as well as wavenumber-frequency domain. Furthermore, the wavenumber-frequency domain implementation is more efficient compared to the space-frequency domain implementation ; in the space-frequency domain, a two-dimensional horizontal convolution must be carried out, while in the wavenumber-frequency domain, a multiplication has to be carried out. The implementation of the inverse wavefield extrapolation in the wavenumber-frequency domain requires a regular sampling of the measured data. An overview of the specific domain-related properties of the different implementations is given in Table 2. When the inverse extrapolator is calculated in the space-frequency domain, while the actual inverse extrapolation is carried out in

Table 2. Overview of the Advantages and Disadvantages of the Different Domains of the Implementation of the Scalar Wavefield Extrapolators

	Domain of implementation		
	Space-frequency	Wavenumber-frequency	
Irregular sampling	+	−	−
Topographic correction	+	−	−
Efficiency	−	+	+
Frequency-dependent medium parameters	+	+	+

the wavenumber-frequency domain, we speak of a combined space-frequency wavenumber-frequency implementation. This is indicated in the table by the middle column and will be the way the multi-component inverse extrapolator is calculated.

5.4. Multi-Component Inverse Wavefield Extrapolator

It has been shown in [18] that single-component inverse wavefield extrapolators based on the forward wavefield extrapolator for a homogeneous space are not bounded, and that the inverse wavefield extrapolation has to be carried out by combining more components of the measured scattered electric field. To combine more components of the emitted and measured electric field, a multi-component scattering formalism was achieved by converting Eq. (16), which describes the components $\hat{E}_{\alpha\beta}$ individually, into a matrix:

$$\hat{\mathbf{E}}(\boldsymbol{x}^M, \omega) = \hat{S}(\omega) \int_{\boldsymbol{x}^c \in \mathbb{D}^s} \hat{\mathbf{D}}(\boldsymbol{x}^M - \boldsymbol{x}^c, \omega) \boldsymbol{\chi}^{\hat{\eta}}(\boldsymbol{x}^c)\, dV. \tag{29}$$

where $\hat{\mathbf{E}}(\boldsymbol{x}^M, \omega)$ is given by

$$\hat{\mathbf{E}}(\boldsymbol{x}^M, \omega) = \begin{bmatrix} \hat{E}_{11} & \hat{E}_{12} \\ \hat{E}_{21} & \hat{E}_{22} \end{bmatrix} (\boldsymbol{x}^M, \omega), \tag{30}$$

and $\hat{\mathbf{D}}(\boldsymbol{x}, \omega)$ is the corresponding 3D forward wavefield extrapolator for zero-offset, which is given by

$$\hat{\mathbf{D}}(\boldsymbol{x}, \omega) = \hat{\mathbf{A}}(\boldsymbol{x}, \omega) \exp(-2jkR), \tag{31}$$

where

$$\hat{\mathbf{A}}(\boldsymbol{x}, \omega) = \begin{bmatrix} \hat{A}_{11} & \hat{A}_{12} \\ \hat{A}_{21} & \hat{A}_{22} \end{bmatrix} (\boldsymbol{x}, \omega), \tag{32}$$

and $\hat{A}_{\alpha\beta}$ are given by Eqs. (18a–d). Combining Eqs. (20) and (22a–d) the expression for $\tilde{\mathbf{D}}(k_1, k_2, x_3, \omega)$ is obtained as

$$\tilde{\mathbf{D}}(k_1, k_2, x_3, \omega) = \tilde{\mathbf{d}}(k_1, k_2, x_3, \omega) \exp(-jk_3|x_3|), \tag{33}$$

where

$$\tilde{\mathbf{d}}(k_1, k_2, x_3, \omega) = \frac{-2\pi j C(\omega)}{(2k)^3 |x_3|} \begin{bmatrix} (2k)^2 - k_1^2 & -k_1 k_2 \\ -k_1 k_2 & (2k)^2 - k_2^2 \end{bmatrix}. \tag{34}$$

To obtain an approximate inverse of the multi-component 3-D forward wavefield extrapolator $\tilde{\mathbf{D}}(k_1, k_2, x_3, \omega)$, the complex conjugate of

the exponent and the inverse of the matrix in Eq. (34), was taken yielding

$$\tilde{\mathbf{H}}^{\text{inv}}(k_1, k_2, x_3, \omega) = \tilde{\mathbf{h}}^{\text{inv}}(k_1, k_2, x_3, \omega) \exp(jk_3^* |x_3|), \tag{35}$$

where

$$\tilde{\mathbf{h}}^{\text{inv}}(k_1, k_2, x_3, \omega) = \frac{jk|x_3|}{\pi C(\omega) k_3^2} \begin{bmatrix} (2k)^2 - k_2^2 & k_1 k_2 \\ k_1 k_2 & (2k)^2 - k_1^2 \end{bmatrix}. \tag{36}$$

Using the stationary phase approximation, the spatial equivalent of Eqs. (35) and (36) is obtained as

$$\hat{\mathbf{H}}^{\text{inv}} = \frac{4k^2}{4\pi^2 C(\omega)} \begin{bmatrix} (R^2 - x_2^2)/R^2 & x_1 x_2/R^2 \\ x_1 x_2/R^2 & (R^2 - x_1^2)/R^2 \end{bmatrix} \exp(2jkR). \tag{37}$$

Note that the components of this multi-component inverse wavefield extrapolator are bounded.

5.5. Imaging Principle

The approximate inverse of the forward wavefield extrapolator $\hat{\mathbf{D}}$ (see Eq. (29)), which is given by $\hat{\mathbf{H}}^{\text{inv}}$, compensates for all travel times and amplitudes involved in a homogeneous space, including radiation characteristics of the (point) source and (point) receiver. Next, the imaging principle is applied, which states that the data at zero traveltime of the inverse extrapolated recordings, relate to a bandlimited version of the physical property contrasts of the medium of investigation [2,24]. As a consequence, we can simply sum the result for all (positive and negative) frequencies to obtain the imaged contrast in the space domain, such that we can write for the imaged contrast at a specific depth level $\boldsymbol{x} = (x_1, x_2, x_3)$,

$$\langle \chi^{\dot{\eta}}(\boldsymbol{x})\mathbf{I} \rangle = \frac{1}{2\pi} \int \frac{d\omega}{\hat{S}(\omega)} \int_{(x_1^M, x_2^M) \in \mathbb{D}^{SR}} \hat{\mathbf{H}}^{\text{inv}}(\boldsymbol{x} - \boldsymbol{x}^M, \omega) \hat{\mathbf{E}}(\boldsymbol{x}^M, \omega)\, dA, \tag{38}$$

where $\mathbf{I}$ is the unity matrix. Note that the diagonal components $\langle \chi^{\dot{\eta}}(\boldsymbol{x})\mathbf{I} \rangle_{11}$ and $\langle \chi^{\dot{\eta}}(\boldsymbol{x})\mathbf{I} \rangle_{22}$ both return the estimated value of the obtained contrast. According to Eq. (38), each diagonal component ($\langle \chi^{\dot{\eta}}(\boldsymbol{x})\mathbf{I} \rangle_{11}$ and $\langle \chi^{\dot{\eta}}(\boldsymbol{x})\mathbf{I} \rangle_{22}$) consists of the summation of two different measurements ($\hat{E}_{\alpha 1}$ and $\hat{E}_{\alpha 2}$, respectively), which are imaged separately by using appropriate inverse wavefield extrapolators ($\hat{H}_{1\alpha}^{\text{inv}}$ and $\hat{H}_{2\alpha}^{\text{inv}}$, respectively) for that specific measurement.

The foregoing analysis can also be applied for the scalar (single-component) imaging algorithm. Instead of Eq. (29), which was the starting point for the imaging principle for the multi-component imaging algorithm,

the starting point for the imaging principle is given by Eq. (16). Using a similar analysis as carried out to derive the imaging principle for the multi-component imaging, we can now write for the scalar imaging algorithms

$$\chi_{\alpha\beta}^{image}(\boldsymbol{x}) = \frac{1}{2\pi}\int \frac{d\omega}{\hat{S}(\omega)} \int_{(x_1^M,\, x_2^M)\in \mathbb{D}^{SR}} \hat{H}(\boldsymbol{x}-\boldsymbol{x}^M,\omega)\hat{E}_{\alpha\beta}(\boldsymbol{x}^M,\omega)\, dA, \qquad (39)$$

where $\hat{H}$ is an inverse wavefield extrapolator. There are a lot of possible inverse wavefield extrapolators. For example, the inverse wavefield extrapolators for the SAR and the Gazdag algorithms in the space-frequency domain are given by Eqs. (25) and (28), respectively.

5.6. Inverse of Multi-component Wavefield Extrapolator in Two Homogeneous Half-Spaces

Due to the fact that the expressions of the forward wavefield extrapolator were quite elementary in a homogeneous space, an analytical discussion was possible. However, for a homogeneous half-space an analytical approach is not feasible. Nevertheless, a numerical implementation to determine the approximate inverse is still possible. An important benefit is that numerical methods allow the offset between the source and receiver to be taken into account. Similar to Eq. (31), we introduce the forward wavefield operator

$$\hat{\mathbf{D}}(\boldsymbol{x}^M,\boldsymbol{x}^H,\boldsymbol{x}^c,\omega) = \begin{bmatrix} \hat{D}_{11}(\boldsymbol{x}^M,\boldsymbol{x}^H,\boldsymbol{x}^c,\omega) & \hat{D}_{12}(\boldsymbol{x}^M,\boldsymbol{x}^H,\boldsymbol{x}^c,\omega) \\ \hat{D}_{21}(\boldsymbol{x}^M,\boldsymbol{x}^J,\boldsymbol{x}^c,\omega) & \hat{D}_{22}(\boldsymbol{x}^M,\boldsymbol{x}^H,\boldsymbol{x}^c,\omega) \end{bmatrix}, \qquad (40)$$

where $\hat{D}_{\alpha\beta(}\boldsymbol{x}^M,\boldsymbol{x}^H,\boldsymbol{x}^c,\omega)$ is given by Eq. (15). To determine the forward wavefield operator, the different components of the Green's tensor functions can be calculated using the total-field expressions or the far-field expressions (Fig. 2).

The inner product of two vectors of the Green's tensor function (see Eq. (40)) must be determined for each midpoint position $\boldsymbol{x}^M$ (note that $\boldsymbol{x}^H$ is fixed). Then, a two-dimensional spatial Fourier transformation must be carried out. For each k_1, k_2 combination, an inverse matrix can be numerically determined, which results in a representation of the inverse wavefield extrapolator in the wavenumber-frequency domain (Table 2). This calculation using total-field expressions is not yet feasible for imaging of experimental data, because of the large computing time that is needed. The effect of using the far-field expressions instead of the total-field expressions to obtain an inverse wavefield extrapolator are investigated by imaging a point scatterer. Note that for $\hat{\mathbf{H}}^{inv}(\boldsymbol{x}^M,\boldsymbol{x}^H,\boldsymbol{x}^c)$ to be bounded, the inverse wavefield

extrapolator is only determined in the propagating wave region and the evanescent wave region is neglected (see also Eq. (21)).

6. Spatial Resolution Functions

The performance of the scalar and multi-component 3-D inverse wavefield extrapolators was investigated in [18]. The imaging result of a point scatterer was analyzed for one single frequency component, which was denoted as the spatial resolution function. For the special situation of one diffraction point only at position $\boldsymbol{x}^d$, that has a real-valued contrast with unit amplitude yields

$$\chi^{\hat{\eta}}(\boldsymbol{x}) = \delta(\boldsymbol{x} - \boldsymbol{x}^d). \tag{41}$$

A representative resolution function will return also a real-valued resolution function. In [18] it was shown that the resolution function in a homogeneous space using the SAR operator returns a real-valued resolution function with a negative peak, whereas the Gazdag operator returns an imaginary resolution function. The multi-component operator returns a real-valued resolution function with a positive peak giving a representative image of the point scatterer. Closed-form expressions were derived for the spatial resolution functions for the Gazdag and the multi-component inverse wavefield extrapolators using far-field expressions of the electric field. In Table 3, the specifications of the obtained spatial resolution functions are given. For the multi-component inverse extrapolator, an equal spatial resolution for the x_1 and the x_2-axis is obtained, while for the Gazdag inverse extrapolator better resolution is obtained along the x_2-axis than along the x_1-axis. Since a closed-form expression for the SAR spatial resolution function cannot be derived, the widths of its main lobes cannot be analytically determined.

6.1. Modified Scalar Inverse Wavefield Extrapolators

An important requirement of an inverse wavefield extrapolator is to compensate for the propagation effects. Table 3 shows that the Gazdag

Table 3. Width of the Main Lobe (Measured at the First Zero) for the Resolution Function at the Depth Level of the Diffractor Using the Closed-Form Expressions

Inverse extrapolator	Width of the main lobe		Proportional to
	x_1-plane	x_2-plane	
SAR			$C/2k$
Gazdag	0.84λ	0.60λ	$-jC/\lvert x_3^d \rvert$
Multi-component	0.64λ	0.64λ	$k/2\pi$

Table 4. Overview of the Different Modified Inverse Wavefield Extrapolators in Space-Frequency and Wavenumber-Frequency Domain

Inverse extrapolator	$\boldsymbol{x}-f$ domain $\hat{H}$	$\boldsymbol{k}-f$ domain $\tilde{H}$
SAR	$-\exp(j2kR)$	$\frac{-4\pi jk\lvert x_3\rvert}{(k_3^*)^2}\exp(jk_3^*\lvert x_3\rvert)$
Gazdag	$\frac{-k\lvert x_3\rvert^2}{\pi R^2}\exp(j2kR)$	$-j\lvert x_3\rvert\exp(jk_3^*\lvert x_3\rvert)$

inverse wavefield extrapolator does not satisfy this requirement, because the obtained image is still depending on the depth $|x_3^d|$. Therefore, it is suggested to introduce a modified operator which does compensate for the propagation effects. This is simply achieved by a scaling with $|x_3^d|$. Another requirement was that the obtained image represents the scatterer adequately. The peaks of the results obtained with both scalar inverse extrapolators do not represent the nature of the physical property contrast of the point scatterer. Therefore, modified extrapolators are introduced, which render a more representative reconstruction of the point scatterer. The modified SAR operator consists of the original SAR extrapolator multiplied by -1 to obtain a real-valued resolution function with positive peak. The modified Gazdag operator consists of the original Gazdag extrapolator multiplied with $|x_3^d|$. Also, multiplication with $-j$ is required to obtain a real-valued resolution function with a positive peak. The adjusted extrapolators are given in Table 4 (compare with Table 1). Note, that the amplitudes of the resolution functions are proportional to $-C/(2k)$ and $-C$ for the modified SAR and Gazdag operators, respectively.

6.2. Spatial Resolution Functions for point Scatterer in a Homogeneous Space

The results from Table 3 were obtained by carrying out an analytical analysis using far-field expressions for a scatterer in a homogeneous space. A numerical analysis is now carried out by calculating the response for a point scatterer using the total-field expressions. Next, this data is imaged using the modified SAR, modified Gazdag and the multi-component inverse wavefield extrapolators. The multi-component imaging algorithm is implemented by using the far-field expressions as given in Eqs. (31) and (32).

Figure 7(a) shows the normalized real part of the spatial resolution functions using the modified SAR, modified Gazdag, and the Multi-component inverse wavefield extrapolators for $f = 500$ MHz for a point scatterer

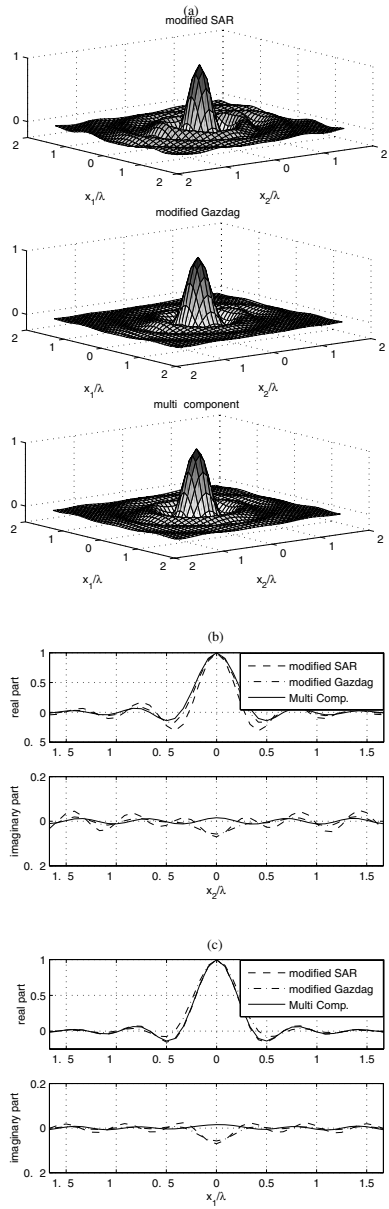

Figure 7. (a) Comparison of normalized real part of spatial resolution function using modified SAR, modified Gazdag and multi-component inverse extrapolators in a homogeneous space (b) comparison of normalized real and imaginary part along x_1-axis, and (c) along x_2-axis.

present in a homogeneous space at a depth of 1 m. Due to the introduction of the modified scalar inverse wavefield extrapolators, all resolution functions have a positive peak amplitude. Furthermore, it can be observed that the modified SAR and the modified Gazdag image are not circularly symmetric, whereas the multi-component image is circularly symmetric. In Figure 7(b,c) the results using the three inverse extrapolators are compared along the x_1- and the x_2-axis, respectively.

As already indicated in Table 3, the width of the main lobe along the x_1-axis is larger for the modified Gazdag operator and similar for the modified SAR compared to the multi-component image. Both scalar images have a relatively large imaginary value. They have a smaller width of the main lobe along the x_2-axis, and thus a higher resolution, compared with the multi-component image. The amplitude of the oscillations along the x_2-axis obtained with the modified SAR image is quite significant.

The multi-component image shows a circularly and mainly real-valued resolution function. The multi-component inverse wavefield extrapolator eliminates the propagation effects in an accurate way, because the far-field expressions are a good approximation of the total-field expressions (Fig. 1(b,c)).

6.3. Modified Scalar Inverse Wavefield Extrapolators for Non-zero Offset between Source-Receiver

From the expressions for the modified operators given in Table 4, it can be observed that it is not feasible to take into account the offset $2\boldsymbol{x}^H$ between the source and receiver antennas when the operators are implemented in the wavenumber-frequency domain. However, in the space-frequency domain the offset between the source and receiver antennas can be incorporated in an approximate sense as follows:

$$\hat{H}^{\mathrm{sar}}(\boldsymbol{x}^M, \boldsymbol{x}^H, \boldsymbol{x}^c, \omega) = j\exp(jkR^S) \times j\exp(jkR^R), \tag{42a}$$

$$\hat{H}^{\mathrm{gd}}(\boldsymbol{x}^M, \boldsymbol{x}^H, \boldsymbol{x}^c, \omega) = j\sqrt{\frac{k}{\pi}}\frac{|x_3^d|}{R^S}\exp(jkR^S) \times j\sqrt{\frac{k}{\pi}}\frac{|x_3^d|}{R^R}\exp(jkR^R), \tag{42b}$$

where

$$R^S = |\boldsymbol{x}^M - \boldsymbol{x}^H - \boldsymbol{x}^d|, \tag{43a}$$

$$R^R = |\boldsymbol{x}^M + \boldsymbol{x}^H - \boldsymbol{x}^d|. \tag{43b}$$

In this way, the propagation from source to scatter position and the propagation from scatter position towards the receiver is accounted for by two

separate phase shifts. Note that for the modified SAR-operator, each separate phase shift is supplemented by a factor j, while for the modified Gazdag-operator each separate phase shift is supplemented by a factor which consists of a spatial taper $|x_3^d|/R$ and a frequency-dependent factor k and is given by $j\sqrt{k/\pi}\,|x_3^d|/R$. It is obvious that the two modified operators consist of the appropriate phase shift, whereas it is recommended to check the validity of the amplitude factor of the modified Gazdag phase shift by numerical analysis. There is no physical meaning of the two split one-way amplitude terms in Eq. (42), because the SAR and Gazdag operators were originally developed for scalar imaging purposes.

6.4. Spatial Resolution Functions for a Point Scatterer in Two Homogeneous Half-Spaces

Numerical analysis is carried out for a point scatterer present in a homogeneous half-space. The point scatterer is present at a depth of 1 m. The scattered electric field is calculated using total-field expression obtained by evaluating the integral expressions for a real-valued contrast with unit amplitude (see Eq. (41)).

In Figure 8(a), the normalized real and imaginary parts of the modified SAR image are shown. A non-circularly symmetric resolution function is obtained. Note that also a non-zero imaginary part is obtained. In Figure 8(b) the real and imaginary parts of the modified Gazdag image are shown. Again, a non-circularly symmetric resolution function is obtained and a non-zero imaginary part is obtained. Note that the modified SAR image has more oscillations in the tails of the resolution function compared to the Gazdag image (see Fig. 7(b,c) and Fig. 9). These oscillations can be explained by the amplitude of the modified SAR operator being not bounded for horizontal wavenumbers when approaching the boundary between the propagating and evanescent wave region (see Eq. (26)).

In Figure 8(c) the normalized real and imaginary parts of the multi-component image using the far-field expressions are shown. The obtained resolution function is more circularly symmetric than the scalar images. The imaginary part for the multi-component image has smaller amplitudes than the scalar images. Note that the use of the far-field expressions, which are used to perform the inverse wavefield extrapolation, do not completely correct for the propagation of the total electric field for a scatterer present at 1 m depth, due to the fact that an error exists between the total field and the far field, as is shown in Figure 2(b–d) and Figure 6(a,b). This results in the real part not being completely circularly symmetric and the imaginary part of the obtained image being unequal to zero.

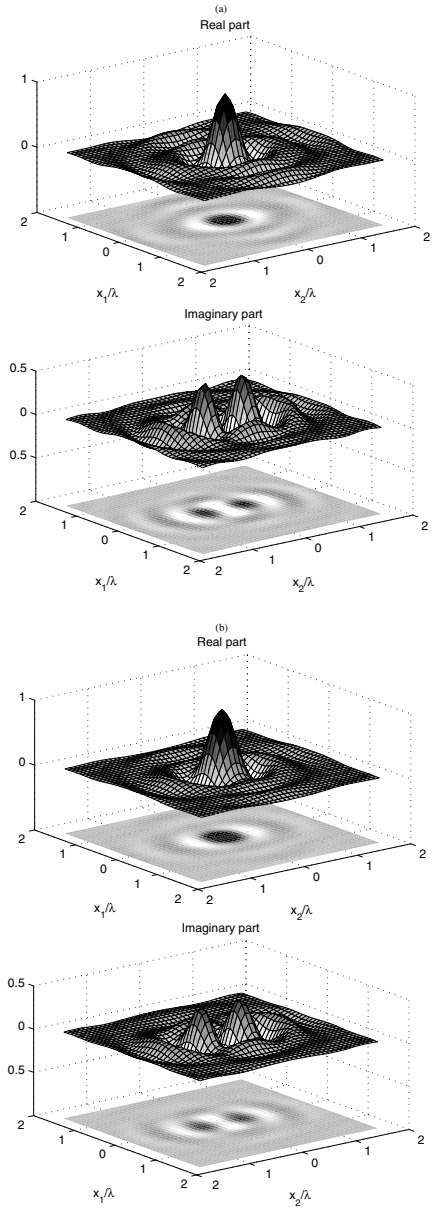

Figure 8. Normalized real part and imaginary part of spatial resolution function in two homogeneous half-spaces using the (a) modified SAR and (b) modified Gazdag imaging algorithm and using the multi-component imaging algorithm using the (c) far-field, and the (d) total-field expressions to calculate the inverse wavefield extrapolator.

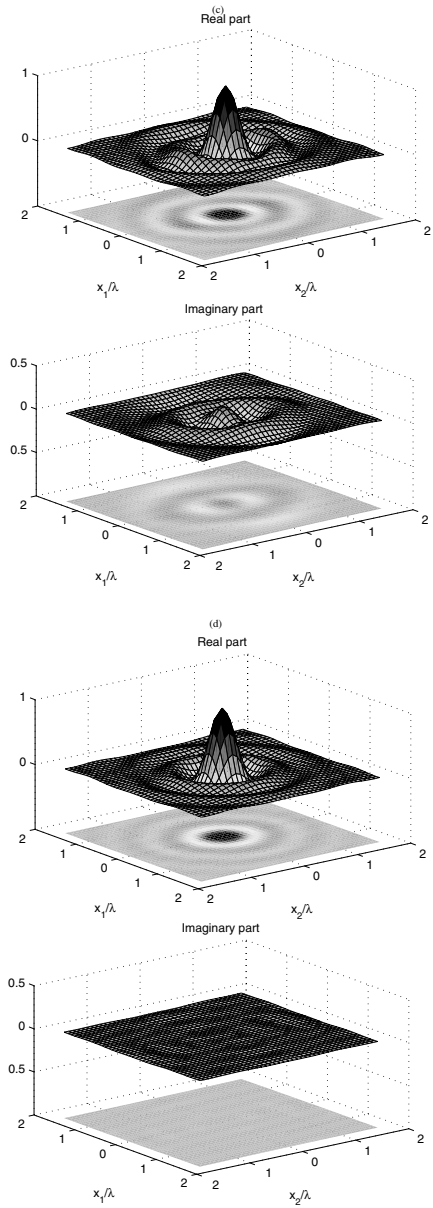

Figure 8. Continued.

In Figure 8(d) the normalized real and imaginary parts of the multi-component image using the total-field expressions are shown. The resolution function shows a realistic positive real-valued circular symmetric image and represents the properties of the point scatterer, which has a positive real-valued contrast.

The scalar images and multi-component image obtained using far-field expressions are compared along the x_1- and the x_2- plane in Figure 9. It can be observed that the peaks in the tail for the real part of the multi-component image are located at the same position relative to the maximum, while for the modified SAR and the modified Gazdag images the peaks are located at different positions on the x_1 and the x_2 axes. This again indicates that the multi-component image is more circularly symmetric than the single-component images. The difference in the width of the main lobe for the three imaging algorithms is not as large as in the homogeneous case (see Fig. 7(b,c)). However, significant imaginary values are obtained for the scalar imaging algorithms. Due to the fact that not only a maximum real part is obtained for a real-valued contrast, a phase difference is obtained compared with the expected result, which should be only real valued. The maximum obtained for the modified SAR image has a phase difference of 17° with the angle of the actual real-valued contrast (0°). The maximum for the modified Gazdag image has a phase difference of 9° and the multi-component image has a phase difference of −8°. Note that the phase errors are larger over the whole range for the modified SAR and modified Gazdag images than for the multi-component image.

Using the scalar imaging algorithms, different resolution functions are obtained for the homogeneous space and homogeneous half-space, because they are not using the appropriate Greens functions. The multi-component imaging algorithm is based on an approximate inverse in the spatial Fourier domain of the forward wavefield extrapolator. Because this extrapolator consists of the appropriate Greens functions, similar resolution functions are obtained in both a homogeneous medium and homogeneous half-space.

It is not feasible to use the total-field expressions for real applications because that needs an enormous amount of computing time. The far-field expressions are used for the multi-component imaging algorithm to image the experimental data.

7. Experimental Results

7.1. Description of the Measurements

For controlled experiments, a testing site has been constructed in Scheveningen located near the coast in the Netherlands. Several steel pipes

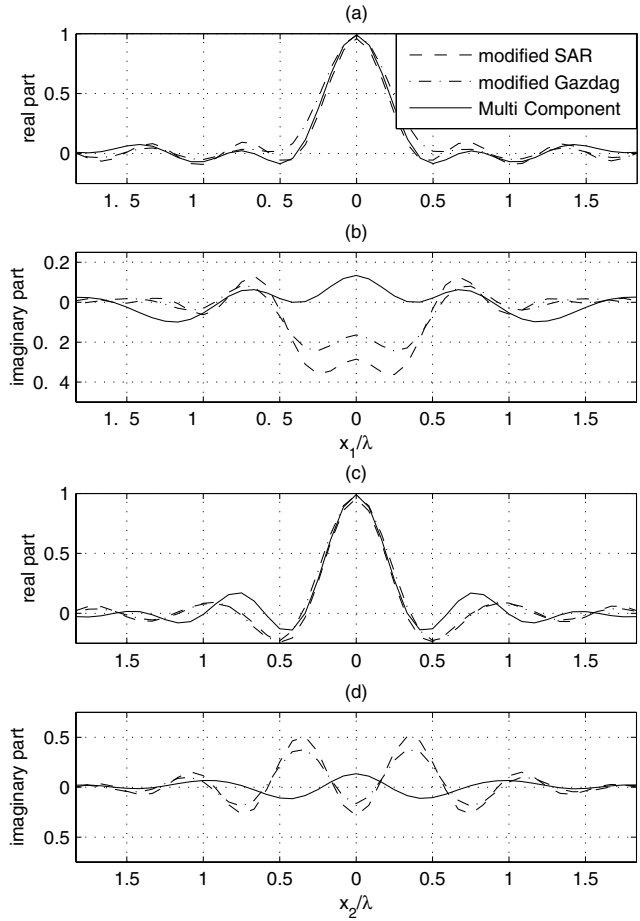

Figure 9. (a) Perspective view of the multi-component image $\langle \chi^{\dagger\eta}(\boldsymbol{x})\mathbf{I}\rangle_{11}$ using pulseEKKO 900 MHz antennas in the perpendicular–broadside configuration and the perpendicular–parallel inline-configuration. Analysis of normalized real, imaginary part and absolute value of the image (b) for the metal pipe (A) along the dashed line parallel to the x_1-axis and (c) for the plastic sphere (F) along a dash-dotted line parallel to the x_2-axis, respectively.

were buried with a different orientation with respect to the survey lines. One plastic and several metallic spheres were also buried in the sand. The multi-component measurements were carried out on a survey grid consisting of 60 lines with an inline and crossline spatial sampling of $\Delta x_1^M = \Delta x_2^M = 5$ cm. The survey lines are oriented in the x_2-direction. The offset between the source and receiver antennas was $2\Delta x_2^H = 35$ cm, which was

(a) Perpendicular-broadside (co-pole)

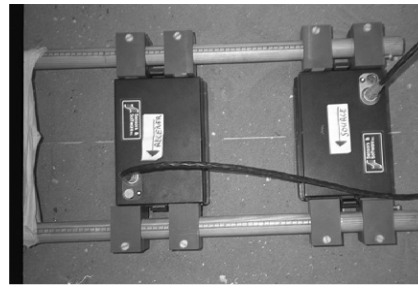

(b) Perpendicular-Parallel (cross-pole) inline

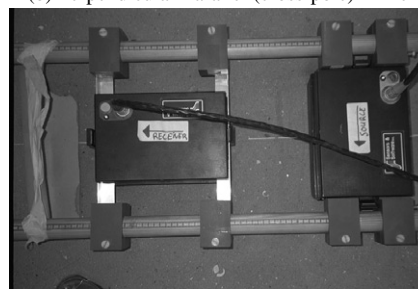

Figure 10. Two inline orientations in a rigid frame used for the multi-component experiments with an offset of 35 cm.

chosen in such a way that for all orientations no clipping of the measured electric field occurs. Measurements were made with the pulseEKKO 1000 system using the 900 MHz antennas. A stacking fold of 16 was used to increase the signal-to-noise ratio. The temporal sampling interval was 50 ps, which was used to obtain 1000 samples, which resulted in a time window of 50 ns. The actual multi-component measurements were carried out using the two inline source-receiver combinations as depicted in Figure 10. The scattered electric field measured in the perpendicular-broadside configuration and the perpendicular–parallel inline-configuration are represented by E_{11} and E_{21}, respectively.

7.2. Three-Dimensional Imaging Results

First of all, the measured data of the different survey lines are aligned by using the maximum and minimum values of the direct air wave. Our imaging algorithm assumes that only scattered data are measured. In reality, direct waves are also measured, the air- and ground-wave. To remove these

direct waves, which are equal for each measurement in the case of a homogeneous top layer, a simple average subtraction is carried out. The data were imaged using an effective relative permittivity for the lower homogeneous half-space of $\varepsilon_r = 3.1$. The offset between the source and receiver was taken into account. The radiation patterns in a homogeneous half-space was only taken into account by the multicomponent imaging algorithm.

The multi-component imaging algorithm combines the two measurements of E_{11} and E_{21}, which results in the contrast quantity $\langle \chi^{\dagger\eta}(\boldsymbol{x})\mathbf{I}\rangle_{11}$ derived from Eq. (38). The modified SAR and modified Gazdag images are calculated using Eq. (39) The imaging given in Eqs. (38) and (39) is performed using a summation of 45 frequencies in the range of 100–960 MHz, which has been carried out for positive frequencies only. This facilitates the analysis of real and imaginary parts of the obtained contrast, separately. In our analysis, the source wavelet is not taken into account. As a consequence, the properties of the scattered objects cannot be extracted using the multi-component imaging algorithm. However, the separate analysis of real and imaginary parts, is the most appropriate way to investigate differences between the different imaging algorithms.

7.3. Equi-Amplitude Surfaces for the Multi-Component Imaging Results in a Three-Dimensional Volume

To obtain an overall picture of the obtained results, surfaces of constant absolute value in the image domain were used to depict the different objects in a representative way. The threshold for this surface of constant amplitude must be chosen relative to the maximum amplitude of the object. Because the imaged contrast of the different objects had different maximum amplitudes, different thresholds were used. In Figure 11, the results are depicted. The metal pipes A and B have the largest amplitude and the plastic sphere ***F*** has the smallest amplitude. Some other anomalies are present, which have amplitudes comparable with the amplitude of the imaged plastic sphere (***F***). Note that the equi-amplitude results are only shown to give an overall view of the different objects present at the testing site.

7.4. Comparison between the Imaging Algorithms along a Line

The original SAR algorithm would return an image which would have an opposite sign compared with the results obtained with the multi-component imaging algorithm, whereas the Gazdag algorithm returned an imaged contrast with a maximum value which is approximately 90° out of phase with the multi-component imaging result [18]. The use of the modified

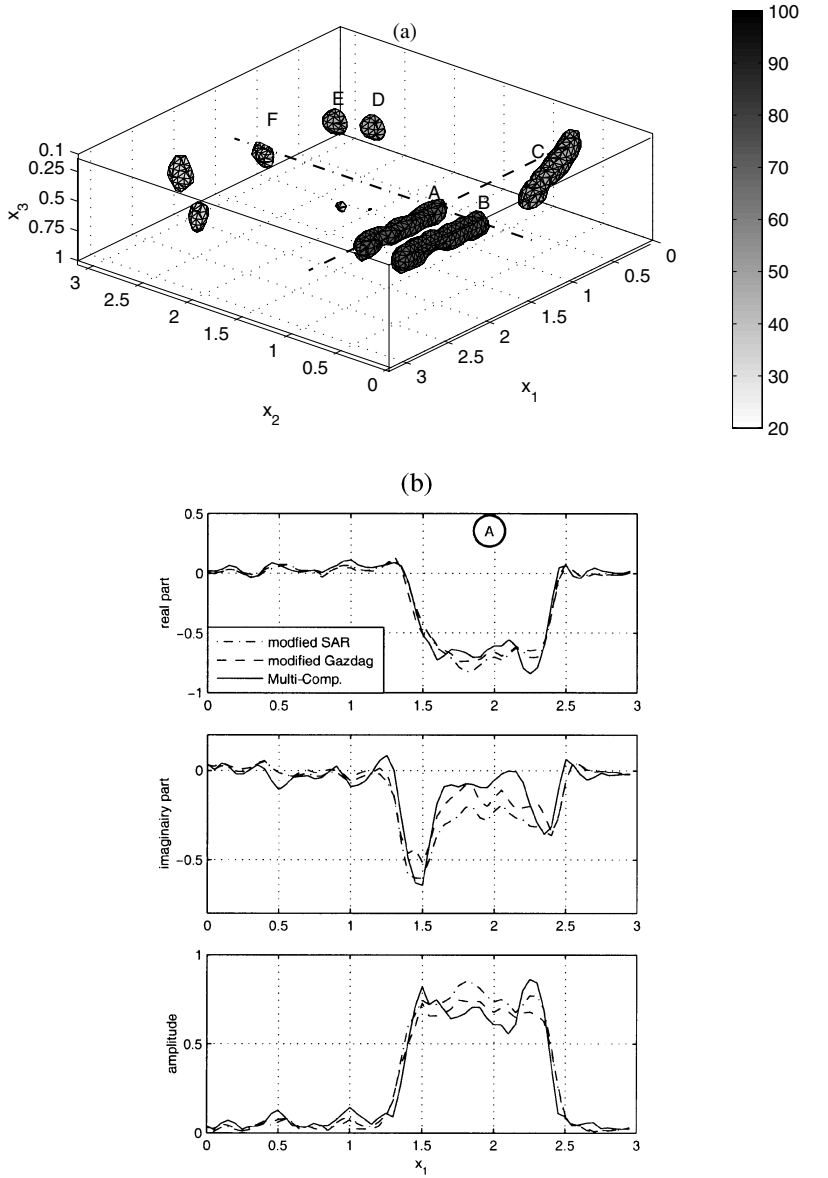

Figure 11. (a) Perspective view of the multi-component image $\langle \chi^{\hat{\eta}}(\boldsymbol{x})\mathbf{I}\rangle_{11}$ using pulseEKKO 900 MHz antennas in the perpendicular–broadside configuration and the perpendicular–parallel inline-configuration. Analysis of normalized real, imaginary part, and absolute value of the image (b) for the metal pipe (A) along the dashed line parallel to the x_1-axis and (c) for the plastic sphere (F) along a dash-dotted line parallel to the x_2-axis, respectively.

(c)

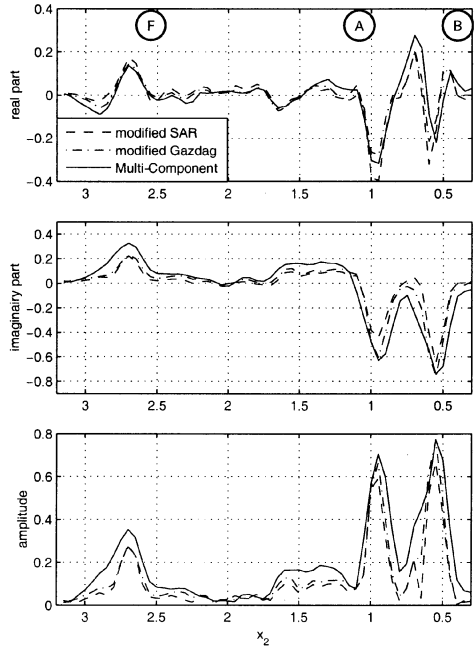

Figure 11. Continued.

SAR and Gazdag algorithms enable a thorough comparison with the multi-component algorithm, because the two modified scalar algorithms return for a certain scatterer an image which approximates better the nature of the physical property contrast of the scatterer than the original scalar algorithms do. Due to the different constants used by the different imaging algorithms, the obtained amplitudes differ. This was already indicated by the results of the resolution functions for a homogeneous space given in Table 1, which are proportional to $k/(2\pi)$, $-C/(2k)$, and $-C$ for the multi-component, the modified SAR and the modified Gazdag operators, respectively. Unlike the scalar images, the multi-component image for a scatterer in a homogeneous half-space can be related with the physical property contrast because the appropriate Greens functions are used to compensate for the propagation effects.

To enable a comparison, the results of the different imaging algorithms are normalized with respect to the maximum absolute value obtained for the multi-component imaging result. The maximum absolute values for the multi-component, modified SAR and modified Gazdag imaging results

were 149, $4.9 \cdot 10^5$ and $2.6 \cdot 10^6$, respectively and were obtained for the image result of steel pipe B. A comparison of the different results is carried out by plotting the obtained amplitudes along a line which intersects an object. Such an analysis is carried out for the metal pipe A and plastic sphere F. In Figure 11(b,c) the real, imaginary and absolute values of the images are plotted for the three imaging procedures, along a line which intersect at the location of object A and F and are parallel to the x_1- and x_2-axis, respectively. These lines are also indicated by the dashed and dash-dotted lines in Figure 11(a). In Figure 11(b), the largest amplitude for object A is obtained for the real part of the imaged contrast for all images. Furthermore it is noted that the imaginary part is small between the endpoints of the pipe for the multi-component image compared with the modified Gazdag and modified SAR image. At position $\boldsymbol{x} = (1.95, 0.95, 0.55)$, the phase of the SAR, Gazdag and multi-component images are $-163°$, $-159°$, and $-171°$, respectively. Thus, the phase of the SAR and the Gazdag images differ with the phase of the multi-component image. In Figure 11(c), a relative large amplitude for object F is obtained for the imaginary part of the imaged contrast compared with the real part for the multi-component image. At position $\boldsymbol{x} = (1.45, 2.7, 0.55)$ the phase of the SAR, Gazdag and multi-component images are $52°$, $58°$, and $67°$, respectively. Again, the phase differences of the SAR and the Gazdag images differ from the phase of the multi-component image. These phase differences indicate the possible error when the properties are determined with the scalar imaging algorithms compared to the multi-component imaging algorithm. Because the multi-component image is calculated using appropriate Greens functions that eliminate the propagation effects, a more reliable image is obtained than with the modified scalar imaging algorithms.

In Figure 11(b), the scalar images have a slightly lower horizontal resolution along the x_1-axis than the multi-component image, whereas in Figure 11(c) the scalar images have a higher horizontal resolution along the x_2-axis. These results are similar to those obtained from our analysis of the spatial resolution functions in a homogeneous space (Table 3 and Fig. 7) and to some extent to the results for a homogeneous half-space (Fig. 9).

Due to the fact that the wavelet is not known, the analysis to obtain the properties of the object is not feasible. However, the phase differences which occur in the experimental data, are similar to the phase differences obtained with the synthetic results.

8. Conclusions

A comparison was made between far-field expressions and the total-field, which was calculated by numerical evaluation of the integral

expressions. For a homogeneous space the far-field is similar to the total field at 3.3λ and $\varepsilon_r = 4$ (Error for $\hat{E}_\phi$ and $\hat{E}_\theta \approx 0.1\%$). The far- and total-field expressions for a dipole present on a homogeneous half-space differ at the critical angle for ≈ 20–25%.

Recently, a multi-component electromagnetic image reconstruction technique was derived, which is based on the vectorial wave equation and takes into account the radiation characteristics of a dipole present in a homogeneous space or half-space. The multi-component image of a point scatterer in a homogeneous space for one single frequency component is a circularly symmetric resolution function. A comparison of the multi-component image of a point scatterer with scalar imaging algorithms, the SAR and the Gazdag imaging algorithms show that the scalar inverse wavefield extrapolators do not result in a representative image of the scatterer. Phase shifts of about 180° and 90° were present between the maxima of the SAR and Gazdag image compared with the multi-component image. In this paper, modified scalar inverse wavefield extrapolators are introduced that minimize these differences. Still the scalar images show no longer a circular and symmetric resolution function, which is an indication that the radiation characteristics of the source and receiver still influence the obtained image for conventional scalar imaging schemes. These differences indicate the possible error in the nature of the physical property contrast when they are determined with the modified scalar imaging algorithms compared to the multi-component imaging algorithm.

For practical imaging strategies, only far-field radiation characteristics can be used in the multi-component imaging algorithm to eliminate the propagation effects due to the large computing time needed to evaluate the total-field expressions for a homogeneous half-space. Synthetic analysis of the imaging of a point scatterer shows that using the far-field expressions in the multi-component imaging algorithm yields a higher quality image than using the modified scalar imaging algorithms. The most circularly symmetric resolution function is obtained for the multi-component image. The multi-component image shows mainly a real-valued reconstruction of the contrast, whereas the SAR and Gazdag images show also imaginary values for the reconstructed contrast. The phase differences were in the order of 10–20°. These phase differences indicate the possible error when the properties are determined with the modified scalar imaging algorithms compared to the multi-component imaging algorithm.

Experimental results of the imaging of several buried objects with different medium properties and different orientations are presented. For the multi-component imaging algorithm, a relatively larger amplitude is obtained for spherical scatterers, compared with the modified scalar images. The phase differences, which occur in the experimental data, are similar to

the phase differences obtained with synthetic results. This indicates that using the multi-component imaging algorithm, a more representative image is obtained than with the modified scalar imaging algorithms.

The next step to determine the medium properties of the scatterers is to take into account the source wavelet and the radiation characteristics of a finite length antenna, including the influence of the intermediate field.

Acknowledgment

This research was supported by the Dutch Technology Foundation (STW), project nr. DMB 3649.

References

1. Davis, J.L. and Anna, A.P., 1989, Ground-penetrating radar for high resolution mapping of soil and rock stratigraphy: Geophysical Prospecting, v. 37, p. 531–551.
2. Berkhout, A.J., 1981, Wave field extrapolation techniques in seismic migration, a tutorial: Geophysics, v. 46, no. 12, p. 1638–1656.
3. Schneider, W.A., 1978, Integral formulation for migration in two and three dimensions: Geophysics, v. 43, no. 1, p. 49–76.
4. Gazdag, J., 1978, Wave equation migration with the phase-shift method: Geophysics, v. 43, p. 1342–1351.
5. Wapenaar, C.P.A. and Berkhout, A.J., Elastic wave field extrapolation: redatuming of single- and multi-component seismic data: Advances in Exploration Geophysics 2. Elsevier Science, Amsterdam, 1989.
6. Mast, J.E. and Johansson, E.M., Three-dimensional ground penetrating radar imaging using multi-frequency diffraction tomography, *in* Proceedings of SPIE The International Society for Optical Engineering, volume 2275, pages 196–203, 1994.
7. Johansson, E.M. and Mast, J.E., Three-dimensional ground penetrating radar imaging using synthetic aperture time-domain focusing, *in* Proceedings of SPIE The International Society for Optical Engineering, volume 2275, pages 205–215, 1994.
8. Grasmueck, M., 1996, 3-D ground-penetrating radar applied to fracture imaging in gneiss: Geophysics, v. 61, no. 4, p. 1050–1064.
9. Lehmann, F. and Green, A. G., 1999, Semi-automated georadar data acquisition in three dimensions: Geophysics, v. 64, p. 836–848.
10. Binningsbø, J., Eide, E.S., and Hjelmstad, J. F., 3D migration of GPR array-antenna data, *in* Proceedings of the Eighth International Conference on Ground-Penetrating Radar, Gold Coast, Australia, pages 459–463, 2000.
11. Lopez-Sanchez, J.M. and Fortuny-Guasch, J., 2000, 3-D radar imaging using range migration techniques: IEEE Transactions on Antennas and Propagation, v. 48, no. 5, p. 728–737.
12. Annan, A.P., Waller, W.M., Strangway, D.W., Rossiter, J.R., Redman, J.D., and Watts, R.D., 1975, The electromagnetic response of a low-loss, 2-layer, dielectric earth for horizontal electric dipole excitation: Geophysics, v. 40, p. 285–298.
13. Engheta, N., Papas, C.H., and Elachi, C., 1982, Radiation patterns of interfacial dipole antennas: Radio Science, v. 17, no. 6, p. 1557–1566.

14. Moran, M.L., Greenfield, R.J., Arcone, S.A., and Delaney, A.J., 2000, Multidimensional GPR array processing using Kirchoff migration: Journal of Applied Geophysics, v. 43, p. 281–295.
15. Lehman, F., Boerner, D., Holliger, K., and Green, A.G., 2000, Multicomponent georadar data: Some implications for data acquisition and processing: Geophysics, v. 65, no. 5, p. 1542–1552.
16. van Gestel, J.-P. and Stoffa, P.L., 2001, Application of Alford rotation to ground-penetrating radar data: Geophysics, v. 66, p. 1781–1792.
17. Wang, T. and Oristaglio, M.L., 2000, GPR imaging using the generalised radon transform: Geophysics, v. 65, no. 5, p. 1553–1559.
18. van der Kruk, J., Wapenaar, C.P.A., Fokkema, J.T., and van den Berg, P.M., Three-dimensional imaging of multicomponent ground-penetrating radar data: accepted for publication in Geophysics.
19. de Hoop, A.T., Handbook of Radiation and Scattering of Waves, Academic Press, Amsterdam, 1995.
20. van der Kruk, J., Three-dimensional imaging of multi-component ground penetrating radar data. PhD Thesis, Delft University of Technology (wwwtg.mp.tudelft.nl/~jvdkruk), 2001.
21. Radzevicius, S.J. and Daniels, J.J., GPR H-plane antenna patterns for a horizontal dipole on a halfspace interface, *in* Proceedings of the Eighth International Conference on Ground-Penetrating Radar, Gold Coast, Australia, pages 712–717, 2000.
22. Holliger, K. and Bergmann, 1998, T., Accurate and efficient modeling of ground-penetrating radar antenna radiation: Geophysical Research Letters, v. 25, p. 3883–3886.
23. Born, M. and Wolf, E., Principles of Optics, Pergamon Press, London, 1965.
24. Claerbout, J.F., 1971, Toward a unified theory of reflector mapping: Geophysics, v. 36, no. 3, p. 467–481.
25. Curlander, J.C. and McDonough, R.N., Synthetic Aperture Radar, Systems and Signal Processing, Wiley series in Remote Sensing, Wiley, New York, 1991.
26. Stolt, R.H., 1978, Migration by Fourier transform: Geophysics, v. 43, no. 1, p. 23–48.